2017

Photosensitization of TiO2 nanofibers by Ag2S with the synergistic effect of excess surface Ti3+ states for enhanced photocatalytic activity under simulated sunlight

Samina Ghafoor
Lahore University of Management Sciences, University of the Punjab

Sadia Ata
University of the Punjab

Nasir Mahmood
University of Wollongong, nmahmood@uow.edu.au

Salman Noshear Arshad
Lahore University of Management Sciences

Photosensitization of TiO2 nanofibers by Ag2S with the synergistic effect of excess surface Ti3+ states for enhanced photocatalytic activity under simulated sunlight

SCIENTIFIC REPORTS

Photosensitization of TiO$_2$ nanofibers by Ag$_2$S with the synergistic effect of excess surface Ti^{3+} states for enhanced photocatalytic activity under simulated sunlight

Samina Ghafoor[1,2], Sadia Ata[2], Nasir Mahmood [3] & Salman Noshear Arshad [1]

TiO$_2$ nanofibers, with mean diameter ~200 nm, were fabricated by electrospinning and successfully photosensitized with low bandgap Ag$_2$S nanoparticles of 11, 17, 23 and 40 nm mean sizes, with corresponding loading of 4, 10, 18 and 29 wt.% Ag$_2$S, respectively. 17 nm Ag$_2$S@TiO$_2$ nanofibers exhibited optimal activity in the photodegradation of methylene blue under simulated sunlight with pseudo-first order rate constant of 0.019 min^{-1} compared to 0.009 min^{-1} for pure TiO$_2$ nanofibers. In spite of greater visible-light absorption and reduced bandgap, larger than 17 nm Ag$_2$S nanoparticles exhibited sluggish photodegradation kinetics probably due to less photo-induced carriers generation in TiO$_2$ and reduced electron injection rates from the larger sized Ag$_2$S into TiO$_2$. Furthermore, a UV-O$_3$ surface treatment induced excess Ti^{3+} surface states and oxygen vacancies which synergistically enhanced the photodegradation rate constant to 0.030 min^{-1} for 17 nm Ag$_2$S@TiO$_2$ sample which is ~70% better than the previously reported for Ag$_2$S/TiO$_2$ hierarchical spheres. This was attributed to the efficient charge separation and transfer driven by increased visible-light absorption, bandgap narrowing and reduced electron-hole recombination rates. The present study demonstrate the potential utilization of Ag$_2$S@TiO$_2$ nanofibers in filtration membranes for removal of organic pollutants from wastewater.

Hazardous wastewater pollution is becoming a serious threat to human health[1] which necessitates the development of green and efficient water remediation technologies. Visible-light driven photocatalysis using suitable bandgap oxide-based nanomaterials is an effective technique to chemically transform the organic pollutants into non-hazardous compounds[2]. Titanium dioxide (TiO$_2$) is widely used as a photocatalyst because it is non-toxic, chemically and thermally stable and inexpensive with a strong oxidizing ability[3–5]. However, its practical use is limited by very low visible-light activity and high recombination rates of photo-induced electron-hole pairs[6]. The Anatase phase of TiO$_2$ has a bandgap (E$_g$) of 3.2 eV which covers only 3–5% of the solar spectrum. Moreover, TiO$_2$ is commonly used as nanoparticles (NPs) which exhibits low photodegradation rates for many organic pollutants due to agglomeration and low active area loading. Electrospinning is a relatively easy and low cost technique for synthesis of ultra-long TiO$_2$ nanofibers (NFs) and permeable membranes[7] which can facilitate the charge transportation and separation, thus, reducing the recombination rate of electron-hole pairs[8, 9]. In fact, Choi *et al*. has shown that TiO$_2$ NFs exhibit superior photocurrent generation (factor of ~3) and hydrogen production (factor of ~7) compared to TiO$_2$ NPs due to well-ordered and interconnected architecture and inherent meso-porosity which aids in adsorption and desorption of the reactants and products, respectively[10]. Similarly,

[1]Department of Chemistry, Syed Babar Ali School of Science and Engineering, Lahore University of Management Sciences, Lahore, 54792, Pakistan. [2]Institute of Chemistry, University of the Punjab, P.O. Box 54590, Lahore, Pakistan. [3]Institute for Superconducting and Electronic Materials, Australian Institute for Innovative Materials, University of Wollongong, North Wollongong, 2500, Australia. Correspondence and requests for materials should be addressed to S.N.A. (email: salman.arshad@lums.edu.pk)

enhanced photocatalytic activity of electrospun mesoporous TiO_2 nanofibers was demonstrated by CO_2 reduction to renewable hydrocarbon fuels[11].

Many attempts have been made to enhance the photocatalytic activity of TiO_2 under illumination conditions similar to solar light[12, 13]. These include doping transition metal ions such as Fe^{3+} [14, 15], Ni^{2+} & Ti^{3+} [16], Ti^{3+}-doped TiO_2[17, 18] or nonmetal atoms such as N, F and S[19–21], dye-sensitization[22–24], and coupling with a photosensitizer such as g-C_3N_4[25], MFe_2O_4[26], α-Fe_2O_3, Au, Pt and Au/Pt co-catalysts[27–29], CdS[30, 31], MoS_2@zeolite[32], Ag[33] and Ag_3PO_4[34, 35]. The purpose of coupling with a photosensitizer is to enhance the visible-light harvesting and promote charge separation by effective interface charge transfer between the photosensitizer and TiO_2 for which the relative position of the energy band levels are critical. Recently, Ag_2S has gained considerable attention as a photosensitizer for TiO_2[36–41]. Ag_2S is a direct low bandgap semiconductor material ($E_g{\sim}1.0\,eV$) which responds well in the whole solar energy spectrum. The conduction (CB) and valence (VB) bands of Ag_2S are $-0.3\,eV$ and $+0.7\,eV$, respectively, which is very desirable for photosensitization of TiO_2 with corresponding CB and VB of $-0.1\,eV$ and $+3.1\,eV$, respectively[36]. Zhang et al. demonstrated hollow Ag-Ag_2S/TiO_2 composite spheres with superior photocatalytic activity in reduction of Cr (VI) under both UV and visible-light[42]. Gholami et al. reported 15 fold enhancement of photocurrent for free standing TiO_2 nanotube array, each of 125 nm diameter and 4.1 μm length, sensitized by ~17 nm Ag_2S NPs[37]. Shan et al. demonstrated core-shell Ag/Ag_2S NPs on TiO_2 nanowires as a model photoelectrochemical electrode system[38]. Ong et al. used sequential ionic deposition to fabricate Ag_2S NPs on TiO_2 hierarchical spheres. Enhanced simulated solar light driven photocatalytic performance was demonstrated by water splitting with hydrogen production at 708 $\mu molh^{-1}g^{-1}$ and photodegradation of methyl orange with pseudo-first order rate constant of 0.018 min^{-1} [39].

Immobilization of Ag_2S NPs on TiO_2 nanofibers (NF) is expected to give higher number of active sites. Multiple factors contribute to the photosensitization effect of Ag_2S on TiO_2 nanofibers such as (a) Effect of Ag_2S mean size and loading amount on the injection rate of photo-induced electrons into TiO_2 as well as photo-induced carriers generation rate in TiO_2, (b) Effect of Ag_2S mean size, loading and coverage on the light harvesting capability, (c) Effect of chemical interaction between Ag_2S and TiO_2 on possible lowering of the energy bandgap and the recombination rate, and (d) Effect of changing the surface chemical states and defects on TiO_2 (e.g. Ti^{3+} and oxygen vacancies) on the carrier separation and transport. Li et al.[43] deposited different amounts of Ag_2S NPs on TiO_2 nanorod arrays by varying the number of cycles in successive ionic layer absorption and reaction (SILAR) method. They reported an optimum 25 cycle deposition for maximum photocatalytic degradation rates of methylene orange (MO) under visible-light. However, other factors as noted above were not investigated in detail.

In this report, the combined effect of all these factors for photosensitization of TiO_2 nanofibers has been experimentally investigated and optimized. We demonstrate optimal simulated solar light driven photocatalytic activity for TiO_2 NFs sensitized by ~17 nm Ag_2S NPs, loaded at 10 wt.%, with the synergistic effect of enhanced Ti^{3+} chemical states and oxygen vacancies induced by a facile UV-O_3 surface treatment. Moreover, these composite nanofibers were stable over multiple cycles of photodegradation and demonstrate their potential use for water remediation.

Results and Discussion

Morphology, structure and chemical composition.
The morphology with mean sizes and distribution of Ag_2S@TiO_2 NFs are shown in Fig. 1. The uncoated TiO_2 NFs (Fig. 1(a) inset) have a mean diameter of 195 nm and interstices of ~1 μm size, formed by the interpenetrating nanofibers network. The color of the TiO_2 NFs changed instantaneously as they were dipped in the Tollens reagent with addition of 0.05 M dextrose solution indicating the formation of Ag NPs followed by washing with distilled water and ethanol. The mean size of the Ag NPs was controlled by varying the dipping time in the solution from 0.5–4 min. Figure 1(a–d) shows the successful deposition of Ag_2S NPs by nucleation and growth of Ag followed by sulfurization without any structural damage to TiO_2 NFs. The phase and chemical composition of the Ag_2S NPs was confirmed by XPS and XRD as discussed later. The sizes of Ag_2S NPs showed characteristically log-normal distribution with mean number-averaged size of 11, 17, 23 and 40 nm for dipping times of 0.5, 1, 2 and 4 min, respectively. The number-averaged sizes were statistically measured by tracing at least 100 particles, computing their areas, A, and calculating the corresponding area-equivalent diameters, D, assuming spherical shape ($D = \sqrt{4A/\pi}$). The particles remain distinct and approximately spherical for dipping times up to 2 min but most of them coalesce into bigger and mostly irregular particles after 4 min dipping. In this study, the samples will be labelled as x nm-Ag_2S@TiO_2 where 'x' is the mean size of the Ag_2S NPs. The weight percent loading of Ag_2S in the composite nanofibers was determined by inductively coupled plasma optical emission spectroscopy. A standard $AgNO_3$ salt solution of 1–10 ppm was used to calibrate the emission intensity of Ag which fitted linearly with R^2 value of 0.999. The weight fraction of 11, 17, 23 and 40 nm Ag_2S@TiO_2 composite nanofibers was found to be 4, 10, 18 and 29%, respectively, assuming that all the Ag converted to Ag_2S.

TEM images of 11 nm- and 23 nm-Ag_2S@TiO_2 NFs in Fig. 2(a and b) also show uniform deposition of Ag_2S NPs on the NF surfaces. Their sizes are comparable to those measured from the SEM images. The insets show HR-TEM images of Ag_2S NPs near the NF edges. The lattices identified in 11 nm-Ag_2S@TiO_2 correspond to (031) and ($\bar{1}$12) crystallographic planes with d-spacing of 0.212 and 0.178, respectively, whereas the lattice in 23 nm-Ag_2S@TiO_2 correspond to ($\bar{1}$21) crystallographic plane with d-spacing of 0.196 nm. These were also confirmed by the powder XRD scans of Ag_2S@TiO_2 NF samples shown in the Fig. 3(a), where ($\bar{1}$12), ($\bar{1}$21) and (031)[44] signals were easily detected (JCPDS # 14-0072, Ag_2S, monoclinic). The most intense peak at $2\theta = 25.3°$ corresponds to the (101) crystallographic plane and confirms the formation of pure Anatase TiO_2 phase in all the samples[45]. The chemical composition was verified by the full scan XPS of TiO_2, 17 nm-Ag_2S@TiO_2 and 17 nm-Ag_2S@ TiO_2 + UV-O_3 samples as shown in the Fig. 3(b) which confirms the presence of Ti and O in the un-coated samples and additionally, Ag and S, in the coated samples. All the samples showed C 1 s signal which is typical of the
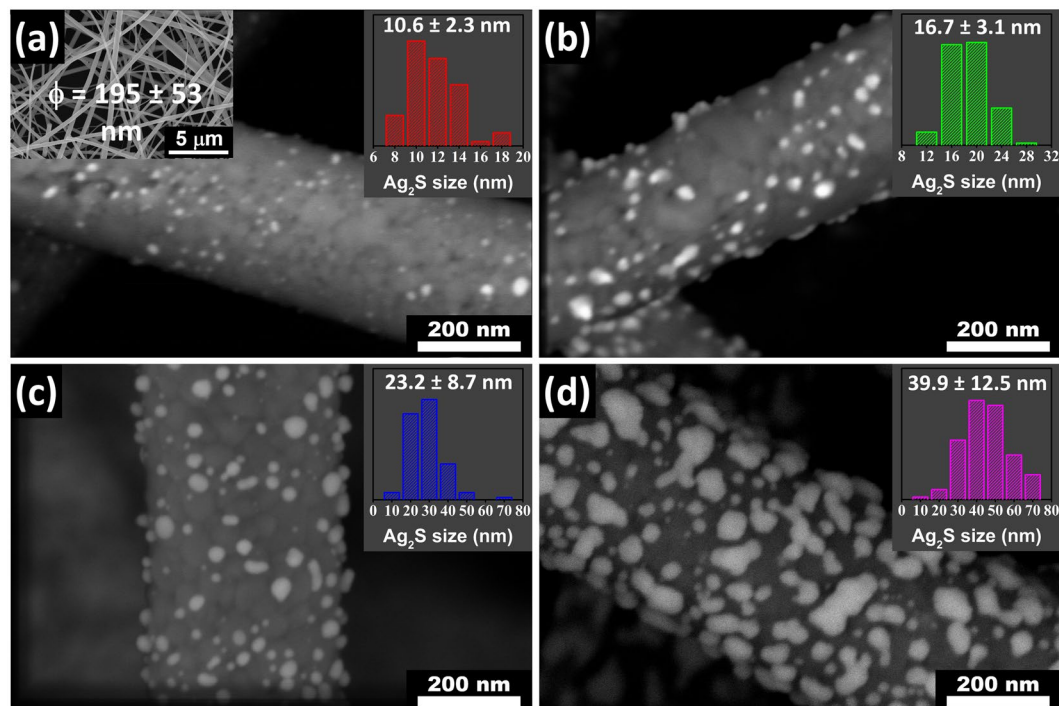
Figure 1. High resolution SEM images of $Ag_2S@TiO_2$ NFs with mean Ag_2S size of (**a**) 11 nm, (**b**) 17 nm, (**c**) 23 nm and (**d**) 40 nm. The Ag_2S size distribution is shown in the insets. A low magnification SEM image of the TiO_2 NFs is also shown as inset in (**a**).
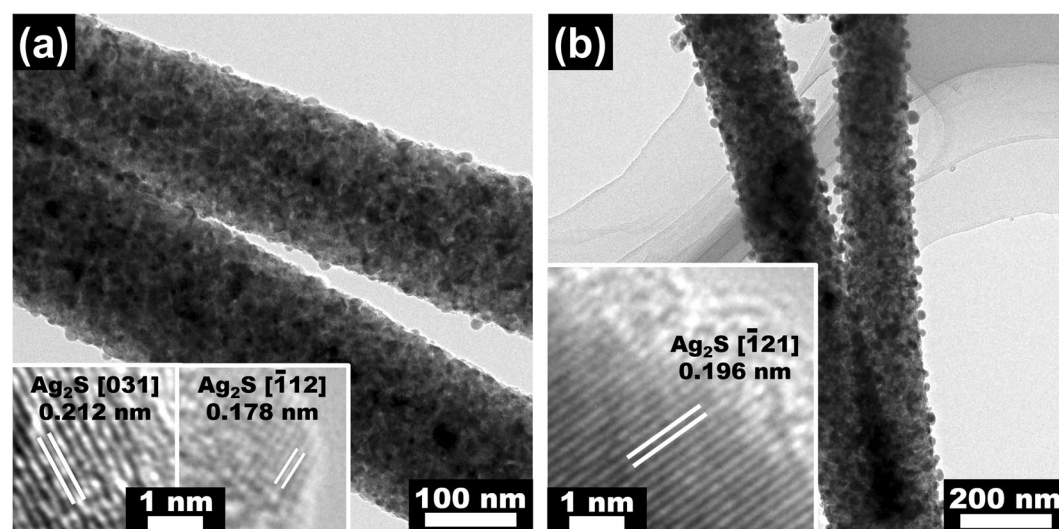

Figure 2. TEM images of (**a**) 11 nm-$Ag_2S@TiO_2$ and (**b**) 23 nm-$Ag_2S@TiO_2$ NFs. Insets are HR-TEM images near the nanofiber edges showing the lattice fringes of the Ag_2S NPs.

adsorbed surface contaminations. The detailed XPS analysis, discussed next, confirmed the presence of Ag_2S on the NF surfaces.

Adsorption-desorption isotherm of pure TiO_2 NFs and 17 nm-$Ag_2S@TiO_2$ composite NFs in Fig. 4(a) closely resembles a type-II isotherm which is typical for non-porous materials due to multilayer formation. The specific surface area of pure TiO_2 NFs and 17 nm-$Ag_2S@TiO_2$ composite NFs was 7.1 and 6.6 m^2/g, respectively, which is consistent with the reported value of 13.3 m^2/g for control TiO_2 nanofibers[46]. The pore size distribution in Fig. 4(b) was calculated by NLDFT method. Absence of hysteresis on desorption branch rules out the presence of mesopores, however, high intake of nitrogen at $P/P_0 > 0.8$ could be attributed to the presence of macropores. Contribution of micropores to the total surface area as calculated by the t-plot method was found to be almost zero.
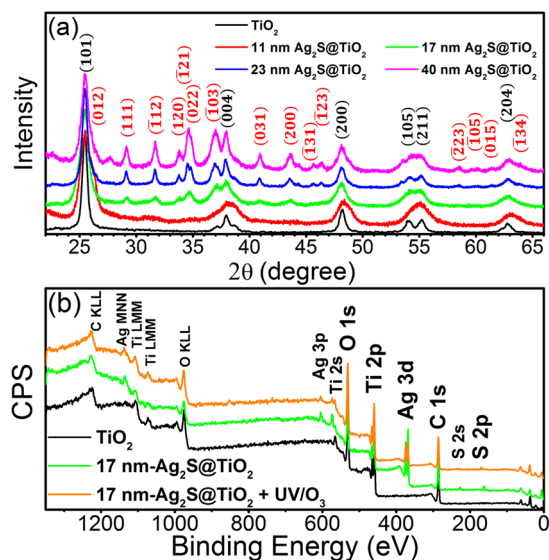
Figure 3. (**a**) XRD scans of pure TiO_2 and $Ag_2S@TiO_2$ NFs. (**b**) Full XPS survey scan of pure TiO_2, 17 nm-$Ag_2S@TiO_2$ and 17 nm-$Ag_2S@TiO_2$ + UV-O_3 samples.
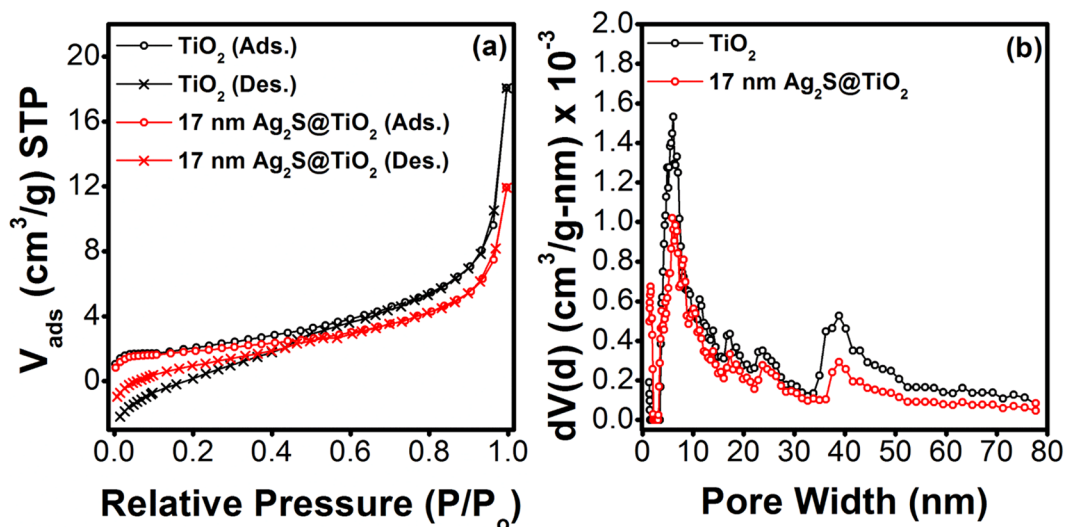
Figure 4. (**a**) Nitrogen adsorption/desorption isotherms for pure TiO_2 NFs and 17 nm-$Ag_2S@TiO_2$ composite nanofibers, and (**b**) the corresponding pore size distributions.

Surface chemical states of $Ag_2S@TiO_2$ nanofibers. The effect of photosensitization by Ag_2S NPs and UV-O_3 treatment on the surface chemical states were determined by XPS. Ti 2p signal of pure TiO_2 NFs had two peaks at 464.1 and 458.4 eV which corresponds to Ti $2p_{1/2}$ and Ti $2p_{3/2}$ spin-orbit splitting, respectively, as shown in the Fig. 5(a). According to the Handbook of X-ray Photoelectron Spectroscopy[47], the binding energies of Ti $2p_{1/2}$ and Ti$2p_{3/2}$ in TiO_2 are 464.3 and 458.8 eV, respectively. The area ratio of these two peaks is ~0.5 (33.67/66.32 = 0.507) with a binding energy difference of ~5.7 eV (464.15–458.46 = 5.69 eV) which is in good agreement with the literature[48]. Ti 2p signal was deconvoluted into four peaks which showed 94.3% Ti^{4+} and 5.7% Ti^{3+} oxidation state on the TiO_2 NFs surface. The Ti^{3+} oxidation state increased to 6.7% after coating with 17 nm Ag_2S NPs which confirms the lower electron density of Ti atoms in $Ag_2S@TiO_2$ NFs. Additionally, the Ti 2p peak positions shifted to higher binding energy indicating the withdrawal of valence electron charge (i.e. oxidation) owing to the strong interaction between Ag_2S and TiO_2 NFs[49]. The UV-O_3 treatment further shifted the Ti 2p peaks towards higher binding energies with increase in Ti^{3+} surface state to 8.2% which indicates the removal of the lattice oxygen. This increase in surface Ti^{3+} had a significant effect on the photocatalytic activity as discussed later.

Deconvolution of O 1s spectra of TiO_2 NFs gave three peaks at 529.7, 531.8 and 533.6 eV, as shown in the Fig. 5(b), which are associated with O^{2-} species in the lattice (TiO_2), oxygen vacancies or defects (Ti^{3+} or Ti_2O_3) and chemisorbed or adsorbed oxygen species, respectively[50]. Similar to Ti 2p, the peaks shifted to higher binding energies after coating with Ag_2S NPs and UV-O_3 treatment. The Ti_2O_3 content increased from 27.4 to 30.2% after
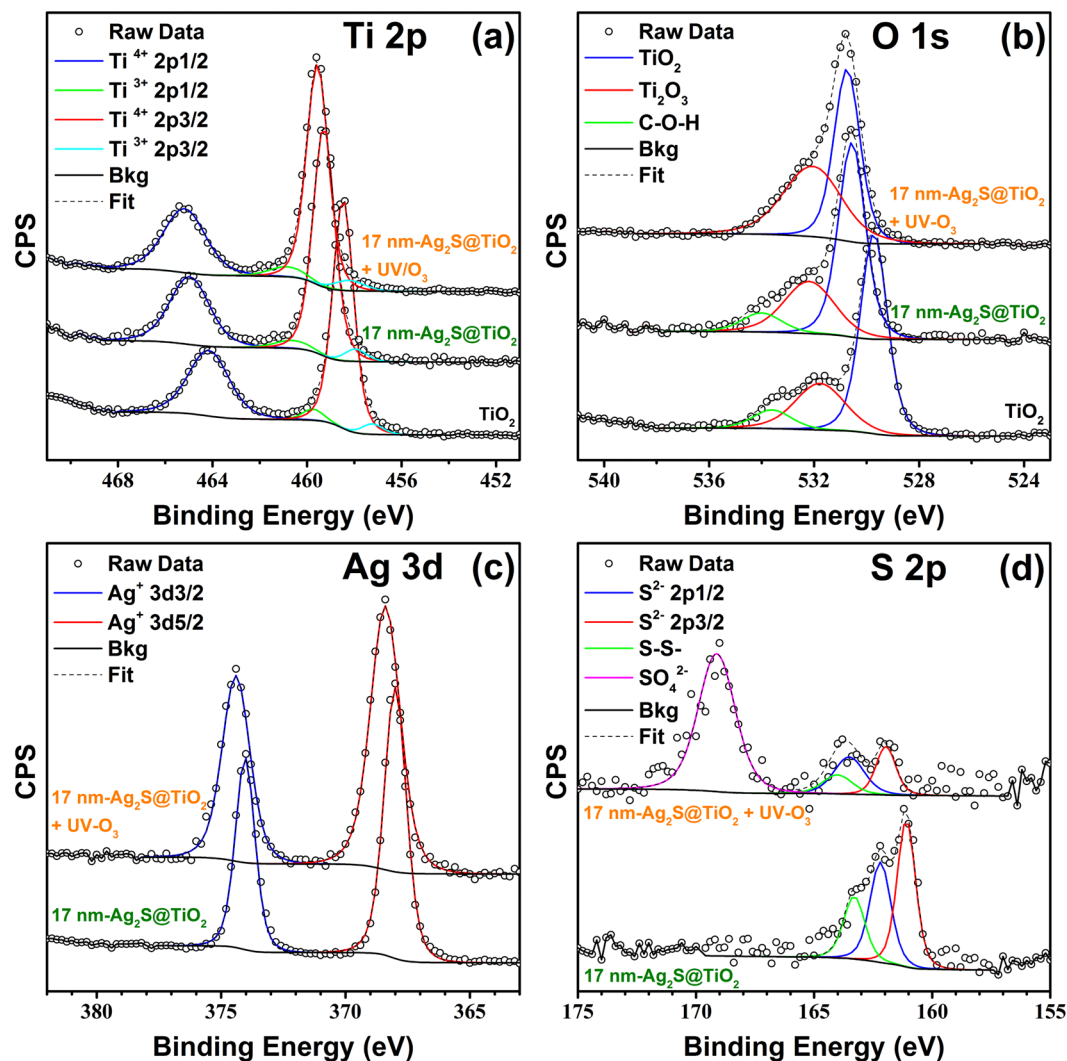
Figure 5. XPS spectra of pure TiO_2, 17 nm-$Ag_2S@TiO_2$ and 17 nm-$Ag_2S@TiO_2$ + UV-O_3 samples. (**a**) Ti 2p, (**b**) O 1 s, (**c**) Ag 3d, and (**d**) S 2p.

coating with 17 nm Ag_2S NPs and further to 47.7% after the UV-O_3 treatment. These results suggest that oxygen vacancies and excess electrons in Ti are generated by this process which results in the reaction $Ti^{4+} \rightarrow Ti^{3+}$ near the surface.

In the Ag 3d XPS spectra, shown in Fig. 5(c), two peaks were observed at 368.0 eV and 374.0 eV representing $3d_{5/2}$ and $3d_{3/2}$ spin-orbit pair, respectively. These peaks were shifted to 368.4 eV and 374.4 eV after UV-O_3 surface treatment and indicated the presence of Ag in Ag^+ form[39, 51]. The S 2p XPS spectra in Fig. 5(d) showed peaks at 161.09 eV and 162.19 eV representing $2p_{3/2}$ and $2p_{1/2}$ of S^{2-} in the metal sulfides, thus, confirming the successful formation of Ag_2S. Another smaller peak at 163.3 eV is assigned to the -S-S- bonding[52] probably due to chemisorption and presence of excess elemental sulfur. These results are in good agreement with the oxidation state of Ag_2S in the literature[53]. Again, these peaks are slightly shifted after UV-O_3 surface treatment with emergence of another peak at 169.12 eV due to SO_4^{2-} formation by the surface oxidation of sulfur.

Photocatalytic performance and mechanism. The Ag_2S mean size, coverage of TiO_2, and UV-O_3 surface treatment had a profound effect on the photocatalytic performance. The photocatalytic activity of $Ag_2S@TiO_2$ NFs were evaluated by monitoring the photodegradation of MB. In a typical experiment, 5 mg of the composite NFs was dispersed in 10 ml of 10 ppm MB solution and kept in dark for 30 min under continuous stirring to attain a complete adsorption-desorption equilibrium[54]. The suspension was then illuminated by a 100 W Xenon arc lamp and photodegradation monitored by the UV-Vis spectrophotometer by measuring the absorbance of MB solution at regular time intervals. The C/C_o as a function of the irradiated time, where C_o is the initial MB solution concentration after the adsorption-desorption equilibrium has been attained, is shown in the Fig. 6(a). All samples showed pseudo-first order photodegradation kinetics with a rate constant of 0.011 min^{-1} for pure TiO_2 NFs which increases to 0.015 min^{-1} and 0.019 min^{-1} after photosensitization by 11 nm and 17 nm Ag_2S NPs, respectively. Remarkably, the rate constant significantly increases to 0.030 min^{-1} after a 2 hr UV-O_3 surface treatment on 17 nm-$Ag_2S@TiO_2$ sample which is ~70% better than 0.018 min^{-1} reported for Ag_2S NPs on TiO_2 hierarchical
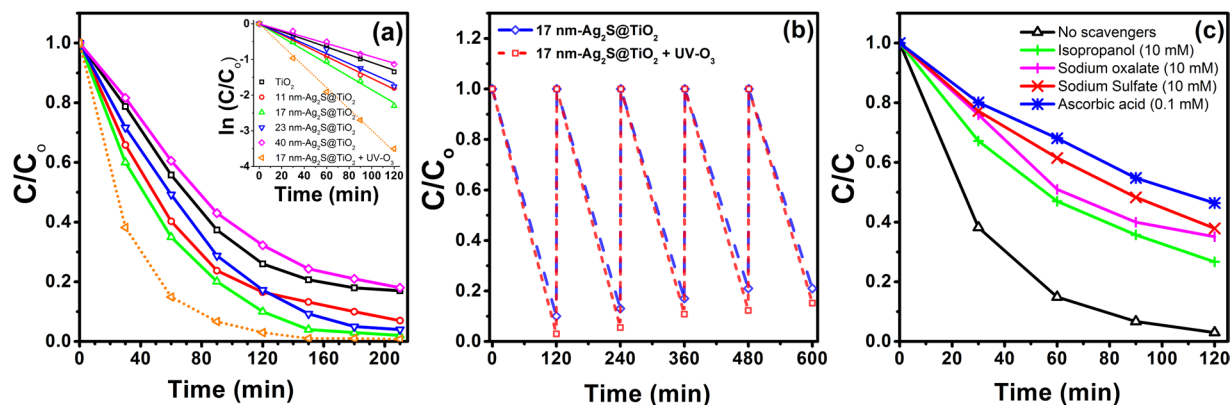
Figure 6. (**a**) Comparative photocatalytic performance (C/C$_o$) of pure and Ag$_2$S sensitized TiO$_2$ NFs under simulated solar light irradiation (inset: pseudo-first order kinetics), (**b**) Photocatalytic performance of 17 nm-Ag$_2$S@TiO$_2$ NFs over 5 cycles, and (**c**) Photocatalytic performance in the presence of radical scavengers.
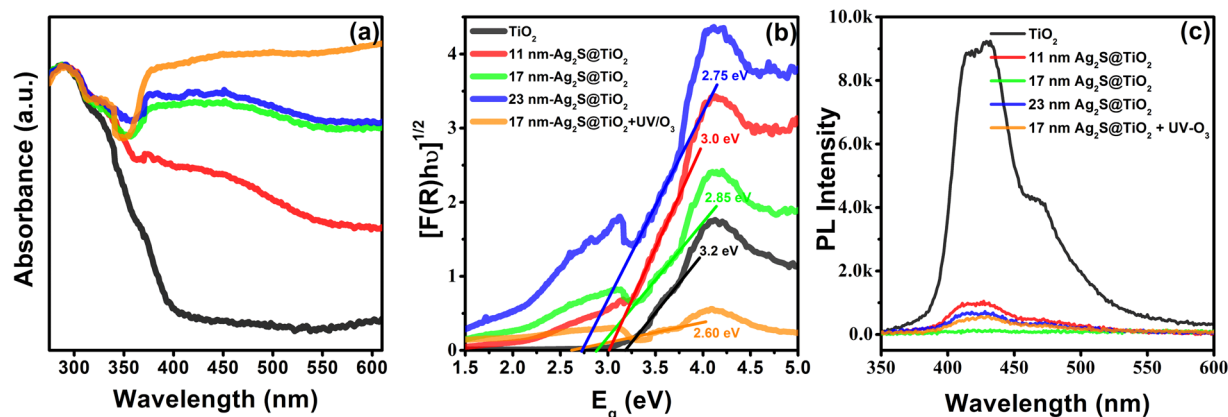

Figure 7. (**a**) UV-vis diffuse reflectance spectra of Ag$_2$S@TiO$_2$ NFs (converted to absorbance), (**b**) Kulbelka-Munk transformation showing the estimated bandgaps, and (**c**) the photoluminescence spectra recorded after 325 nm laser excitation.

spheres[39]. This was attributed to the generation of excess Ti^{3+} surface states and oxygen vacancies, as shown by the XPS results, which facilitated the charge separation process and reduced the electron-hole recombination. We previously reported enhanced photocatalytic activity under UV irradiation for TiO$_2$ NPs (P25 Degussa) loaded polyacrylonitrile NFs due to excess Ti^{3+} surface defects and enhanced hydrophilicity induced by a UV-O$_3$ surface treatment[55]. These NFs showed stable performance when tested over 5 cycles of photodegradation as shown in the Fig. 6(b). Please note that the slight decrease in performance is attributed to ~10% material weight loss during the repeated separation and re-use over 5 cycles. The stability of the samples after photodegradation was investigated by SEM and XRD. The phase, size and loading remained stable with no signs of leaching as shown in the Supplementary Information Fig. 1s.

The radical trapping experiments were carried out to identify the main active oxidation species for photodegradation of MB. As shown in the Fig. 6(c), the photocatalytic efficiencies of the composite nanofibers significantly decreased from 97% to 54%, 62%, 65%, and 73% after the addition of ascorbic acid (as O$_2^{-\bullet}$ scavenger), sodium sulfate (as e$^-$ scavenger), sodium oxalate (as h$^+$ scavenger), and isopropanol (as $^\bullet$OH scavenger), respectively. This indicates that the photoinduced electrons react with dissolved O$_2$ molecules to yield O$_2^{-\bullet}$ radicals, while the positively charged holes (h$^+$) react with OH$^-$ derived from H$_2$O to form $^\bullet$OH radicals. Thus, all these play a significant role in the photodegradation of MB.

Optical properties of Ag$_2$S@TiO$_2$ nanofibers. To investigate the optical response, the absorption spectra of the Ag$_2$S@TiO$_2$ NFs and their corresponding Kulbelka-Munk transformation of the reflectance spectra are shown in Fig. 7(a and b), respectively. Pure TiO$_2$ showed the expected bandgap of 3.2 eV and very weak visible-light absorption. However, the visible-light absorption increased and the bandgap decreased, monotonically, by coating with Ag$_2$S NPs of increasing size due to the enhanced interfacial chemical interaction and coverage of TiO$_2$ by the smaller bandgap (E$_g$~1 eV) Ag$_2$S generating new midgap energy levels. However, the increased size of Ag$_2$S will have a negative impact on the photo-induced carriers generation rate in TiO$_2$ and injection rate of electrons from the conduction band of Ag$_2$S into TiO$_2$, thus, increasing their recombination probability. This was shown by the 23 nm- and 40 nm-Ag$_2$S@TiO$_2$ samples which, despite having a lower bandgap (E$_g$~2.75 eV),
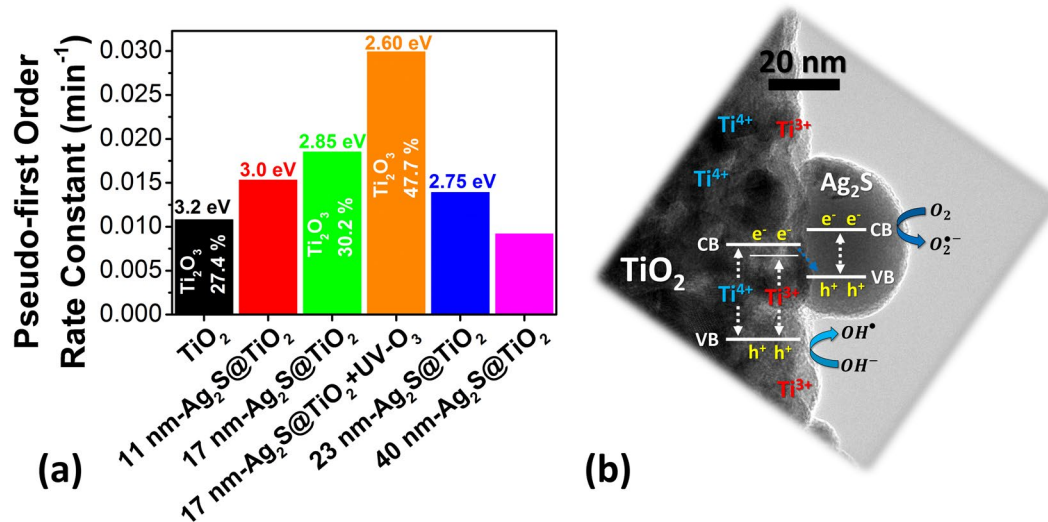
Figure 8. (**a**) Methylene blue photodegradation rate constants for all the samples. Percentage of Ti_2O_3 surface states (estimated form O 1 s XPS signal) and calculated bandgaps are also listed. (**b**) Schematic of the interfacial charge transfer processes during illumination of Ag_2S sensitized TiO_2 nanofibers with excess Ti^{3+} states and oxygen vacancies.

showed even less photocatalytic activity then pure TiO_2 NFs with rate constants of 0.014 and 0.009 min^{-1}, respectively, as shown in the Fig. 8(a). To investigate the promoted charge separation, the samples were excited by 325 nm laser which generates electron-hole pairs. The recombination of these photoexcited carriers gives photoluminescence (PL) signal with an intensity directly proportional to the electron-hole recombination process. Thus, a lower PL is desirable as it indicates a lower charge recombination which will result in a higher photocatalytic activity. As shown in the Fig. 7(c), the pure TiO_2 NF showed a high PL intensity around 425 nm which significantly diminished for Ag_2S photosensitized TiO_2 NFs. Similar PL results are reported for Ag/TiO_2[56] and Ag_2O/TiO_2[57] systems.

The synergistic effect of photosensitization and surface Ti^{3+} states.
The enhanced photocatalytic performance of 17 nm-Ag_2S@TiO_2 + UV-O_3 sample is attributed to the synergistic effect of photosensitization by Ag_2S NPs and excess surface Ti^{3+} states and oxygen vacancies. The proposed effective charge transfer process between Ag_2S and TiO_2 due to the preferred conduction band (CB) and valence band (VB) positions of Ag_2S, which are lower than corresponding bands in TiO_2, is schematically depicted in the Fig. 8(b). This facilitated the generated electrons transfer from CB of Ag_2S to the CB of TiO_2 to effectively inhibit the electron-hole recombination. This photosensitization effect is further supplemented by the high Ti_2O_3 (Ti^{3+} state and oxygen vacancies) near the surface which leads to enhanced absorption of incident solar light below the bandgap of TiO_2 (Ti^{4+} state) as shown in the Fig. 8(b) and reported in ref. 58. The midgap state is close to the CB which facilitates the injection of photogenerated electrons into TiO_2 under simulated solar light. Moreover, the Ti^{3+} defects and oxygen vacancies slows down the electron-hole recombination kinetics by acting as hole traps, thus, prolonging the lifetime of the charges[59].

In summary, photosensitization of electrospun TiO_2 nanofibers was done by Ag_2S nanoparticles with mean sizes of 11–40 nm range for enhanced simulated solar light driven photocatalytic performance. Detailed morphological and structural characterization by SEM, HR-TEM & XRD and chemical states identification by XPS confirmed the growth of Ag_2S nanoparticles. The key characteristics and parameters of all the samples are shown in the Table 1. The size and coverage of Ag_2S had significant effect on the photocatalytic activity with 17 nm-Ag_2S@TiO_2 giving the optimal activity. This was further enhanced by a surface UV-O_3 treatment which introduced excess Ti^{3+} surface defects and oxygen vacancies and reduced the bandgap. This synergistic effect of Ag_2S sensitization and UV-O_3 treatment is attributed to the reduced recombination effect due to efficient charge transfer. The prepared composite NFs were stable in performance when tested over 5 cycles with a maximum photodegradation rate constant of 0.03 min^{-1} for the UV-O_3 treated 17 nm-Ag_2S@TiO_2 nanofibers which is ~70% better than the previously reported value for Ag_2S@TiO_2 hierarchical spheres. These results demonstrate the potential of using these composite NFs for water remediation under sunlight.

Methods
Fabrication of TiO_2 nanofibers.
To fabricate TiO_2 NFs by electrospinning, 1.5 g polyvinylpyrrolidone (PVP, M_w = 1,300,000 g/mol) was mixed in 10 g ethanol and 4 g acetic acid under vigorous stirring for 1 hr. Then 4 g Titanium(IV) n-butoxide (TNBT, 97%) was added in the solution and further stirred for 1 hr to generate a homogeneous electrospinning solution. This precursor solution was electrospun at 18 kV electrical potential with tip to collector distance of 18 cm with pumping rate of 0.8 mL/hr. The non-woven NF mat was left on the aluminum wired collector overnight for complete hydrolysis and annealed in air at 500 °C for 2 hr with a heating rate of 5 °C/min to obtain pure Anatase TiO_2 NFs.

Samples	Ag$_2$S mean size (nm)	Ag$_2$S wt.%	Ti^{3+} (Ti 2p)	Ti^{3+} (O 1 s)	Bandgap (eV)	Rate Constant (min^{-1})
TiO$_2$	—	—	5.7	27.4	3.2	0.011
Ag$_2$S@TiO$_2$ (t$_{dip}$ = 0.5 min)	10.6 ± 2.3	4	—	—	3.0	0.015
Ag$_2$S@TiO$_2$ (t$_{dip}$ = 1.0 min)	16.7 ± 3.1	10	6.7	30.2	2.85	0.019
Ag$_2$S@TiO$_2$ (t$_{dip}$ = 1.0 min) + UV-O$_3$ treated			8.2	47.7	2.60	0.030
Ag$_2$S@TiO$_2$ (t$_{dip}$ = 2.0 min)	23.2 ± 8.7	18	—	—	2.75	0.014
Ag$_2$S@TiO$_2$ (t$_{dip}$ = 4.0 min)	39.9 ± 12.5	29	—	—	—	0.009

Table 1. Material characteristics and photodegradation rate constants for all the samples.

Fabrication of Ag$_2$S@TiO$_2$ nanofibers. Ag$_2$S NPs of different size distribution were grown on TiO$_2$ NFs by a two-step process: reduction of Ag$^+$ to Ag followed by sulfurization of Ag to Ag$_2$S. Typically, 0.1 M NaOH was added drop-wise in 10 mL of 0.01 M AgNO$_3$ solution until appearance of brown precipitates. Then 1.0 M ammonia solution is added drop-wise until dissolution of all brown precipitates which indicates the formation of silver-ammonia complex [Ag(NH$_3$)$_2$]$^+$, commonly known as the Tollens reagent. 10 mL of 0.05 M dextrose solution and 20 mg TiO$_2$ NFs were added into this freshly prepared solution under magnetic stirring, resulting in the formation of Ag NPs. These Ag NPs were then sulfurized to Ag$_2$S[40] by dipping in 25 mL of 0.01 M sulfur/acetonitrile solution at 60 °C for 10 min. The Ag$_2$S@TiO$_2$ NFs were then washed with acetonitrile and distilled water and then dried at 60 °C in oven. The selected Ag$_2$S@TiO$_2$ NFs were also exposed to UV-O$_3$ for 2 hr in a UV-Ozone plasma cleaner chamber.

Characterization. The size and morphology of Ag$_2$S NPs and TiO$_2$ NFs was characterized by field emission scanning electron microscopy (FE-SEM, FEI 450 Nova NanoSEM) and high resolution transmission electron microscopy (HR-TEM, Jeol JEM-2100F operating at 200 kV). The weight fraction of Ag$_2$S in the composite nanofibers was determined by inductively coupled plasma – optical emission spectroscopy (ICP-OES, Perkin Elmer Optima 2100 DV). 3 mg of the sample was digested in 5 mL conc. HNO$_3$ and then diluted up to 50 ml with deionized water. The surface chemical composition and oxidation states of Ti, O, Ag and S were quantified by X-ray photoelectron spectroscopy (XPS, PHI-1600) equipped with Al Kα radiation. The peak positions were calibrated to C 1 s (284.8 eV) and plotted using the CasaXPS software. The photoluminescence spectra of the composite nanofibers were recorded by exciting the samples by 325 nm wavelength laser. The crystalline phases were determined by powder X-ray diffraction (XRD, Bruker D2 Phaser). Diffuse reflectance spectra (DRS) in 200–800 nm range were taken by UV-vis-NIR spectrophotometer (Jasco, V-770) to study the light harvesting capabilities of the samples and estimate their bandgaps using Kubelka-Munk function. The specific surface area was measured using Quantachrome (NOVA 2200 e) surface area and pore size analyzer. Silica kernel with cylindrical pore morphology and NLDFT (equilibrium mode) were used for the calculation of pore volume and pore size. Surface area was measured from nitrogen adsorption-desorption isotherm by applying B.E.T. plot in relative pressure range of 0.05–0.30 P/P$_o$.

Photocatalytic performance. The photocatalytic performance of the Ag$_2$S@TiO$_2$ NFs were evaluated by photodegradation of methylene blue (MB) solution in water. In a typical experiment, 5 mg of the sample was dispersed in a 10 mL solution of 10 ppm MB and kept in dark for 30 min under continuous stirring to attain a complete adsorption-desorption equilibrium on the surface of the composite NFs. Photocatalytic degradation was carried out by illuminating the suspension with simulated solar light using a commercial 100 W Xenon lamp. The analytical sample from the photocatalytic reaction was collected at regular time intervals and centrifuged. The resulting solution was analyzed by recording the absorbance of the residual MB solution with UV-vis spectrophotometer at a wavelength of 662 nm. To identify the active oxidation species responsible for the photocatalytic degradation of MB, a series of radical trapping experiments were carried out. Isopropanol as $^\bullet$OH scavenger (10 mM), ascorbic acid as O$_2$$^{-\bullet}$ scavenger (0.1 mM), sodium sulfate as e$^-$ scavenger (10 mM) and sodium oxalate as h$^+$ scavenger (10 mM) were added directly into the MB solution containing the composite photocatalysts prior to irradiation by simulated solar light.

References

1. Elliott, J. E. & Elliott, K. H. Tracking marine pollution. *Science* **340**, 556–558 (2013).
2. Jing, L., Zhou, W., Tian, G. & Fu, H. Surface tuning for oxide-based nanomaterials as efficient photocatalysts. *Chem. Soc. Rev* **42**, 9509–49 (2013).
3. Chen, X. & Selloni, A. Introduction: Titanium Dioxide (TiO$_2$) Nanomaterials. *Chem. Rev* **114**, 9281–9282 (2014).
4. Wen, J. *et al.* Photocatalysis fundamentals and surface modification of TiO$_2$ nanomaterials. *Cuihua Xuebao/Chinese J. Catal* **36**, 2049–2070 (2015).
5. Sajan, C. P., Wageh, S., Al-Ghamdi, A. A., Yu, J. & Cao, S. TiO$_2$ nanosheets with exposed {001} facets for photocatalytic applications. *Nano Res* **9**, 3–27 (2016).
6. Schneider, J. *et al.* Understanding TiO$_2$ Photocatalysis: Mechanisms and Materials. *Chem. Rev* **114**, 9919–9986 (2014).
7. Teo, W. E. & Ramakrishna, S. A review on electrospinning design and nanofibre assemblies. *Nanotechnology* **17**, R89–R106 (2006).

8. Zhang, F. *et al.* Controllable synthesis of Ag@TiO₂ heterostructures with enhanced photocatalytic activities under UV and visible excitation. *RSC Adv* **6**, 1844–1850 (2016).

9. Chen, Y. L., Chang, Y. H., Huang, J. L., Chen, I. & Kuo, C. Light scattering and enhanced photoactivities of electrospun titania nanofibers. *J. Phys. Chem. C* **116**, 3857–3865 (2012).

10. Choi, S. K., Kim, S., Lim, S. K. & Park, H. Photocatalytic comparison of TiO₂ nanoparticles and electrospun TiO₂ nanofibers: Effects of mesoporosity and interparticle charge transfer. *J. Phys. Chem. C* **114**, 16475–16480 (2010).

11. Fu, J., Cao, S., Yu, J., Low, J. & Lei, Y. Enhanced photocatalytic CO₂-reduction activity of electrospun mesoporous TiO₂ nanofibers by solvothermal treatment. *Dalt. Trans* **43**, 9158–65 (2014).

12. Li, X. *et al.* Engineering heterogeneous semiconductors for solar water splitting. *J. Mater. Chem. A* **3**, 2485–2534 (2015).

13. Etacheri, V., Di Valentin, C., Schneider, J., Bahnemann, D. & Pillai, S. C. Visible-light activation of TiO₂ photocatalysts: Advances in theory and experiments. *J. Photochem. Photobiol. C Photochem. Rev* **25**, 1–29 (2015).

14. Khan, H. & Swati, I. K. Fe³⁺-doped Anatase TiO₂ with d–d Transition, Oxygen Vacancies and Ti³⁺ Centers: Synthesis, Characterization, UV–vis Photocatalytic and Mechanistic Studies. *Ind. Eng. Chem. Res* **55**, 6619–6633 (2016).

15. Yu, H. *et al.* An Efficient Visible-Light-Sensitive Fe (III)-Grafted TiO₂ Photocatalyst. *J. Phys. Chem. C* **114**, 16481–16487 (2010).

16. Zhang, H. *et al.* Ni²⁺ and Ti³⁺ co-doped porous black anatase TiO₂ with unprecedented-high visible-light-driven photocatalytic degradation performance. *RSC Adv* **5**, 107150–107157 (2015).

17. Ren, R. *et al.* Controllable Synthesis and Tunable Photocatalytic Properties of Ti³⁺-doped TiO₂. *Sci. Rep* **5**, 1–11 (2015).

18. Bharti, B., Kumar, S., Lee, H.-N. & Kumar, R. Formation of oxygen vacancies and Ti³⁺ state in TiO₂ thin film and enhanced optical properties by air plasma treatment. *Sci. Rep* **6**, 1–12 (2016).

19. Wang, J. *et al.* Origin of photocatalytic activity of Nitrogen-doped TiO₂ nanobelts. *J. Am. Chem. Soc.* **131**, 12290–12297 (2009).

20. Li, D., Haneda, H., Hishita, S. & Ohashi, N. Visible-Light-Driven N−F−Codoped TiO₂ Photocatalysts. 1. Synthesis by Spray Pyrolysis and Surface Characterization. *Chem. Mater* **17**, 2588–2595 (2005).

21. Zhou, P., Yu, J. & Wang, Y. The new understanding on photocatalytic mechanism of visible-light response NS codoped anatase TiO₂ by first-principles. *Appl. Catal. B Environ* **142–143**, 45–53 (2013).

22. Zhang, M. *et al.* Hierarchical Nanostructures of Copper (II) Phthalocyanine on Electrospun TiO₂ Nanofibers: Controllable Solvothermal-Fabrication and Enhanced Visible Photocatalytic Properties. *ACS Appl. Mater. Interfaces* **3**, 369–377 (2011).

23. Seddigi, Z. S., Ahmed, S. A., Sardar, S. & Pal, S. K. Heterodimerization at the dye sensitized TiO₂ surface: an efficient strategy toward quick removal of water contaminants. *Photochem. Photobiol. Sci* **15**, 920–927 (2016).

24. Kang, X. *et al.* Deposition of loosely bound organic D–A–π–A′ dyes on sensitized TiO₂ film: a possible strategy to suppress charge recombination and enhance power conversion efficiency in dye-sensitized solar cells. *J. Mater. Chem. A* **2**, 11229 (2014).

25. Liu, X. *et al.* A general nonaqueous sol-gel route to g-C₃N₄-coupling photocatalysts: the case of Z-scheme g-C₃N₄/TiO₂ with enhanced photodegradation toward RhB under visible-light. *Sci. Rep* **6**, 39531 (2016).

26. Gao, X., Liu, X., Zhu, Z., Wang, X. & Xie, Z. Enhanced photoelectrochemical and photocatalytic behaviors of MFe₂O₄ (M = Ni, Co, Zn and Sr) modified TiO₂ nanorod arrays. *Sci. Rep* **6**, 30543 (2016).

27. Liu, C. *et al.* Efficiently enhancing the photocatalytic activity of faceted TiO₂ nanocrystals by selectively loading α-Fe₂O₃ and Pt co-catalysts. *RSC Adv* **6**, 29794–29801 (2016).

28. Shuang, S., Lv, R., Xie, Z. & Zhang, Z. Surface Plasmon Enhanced Photocatalysis of Au/Pt-decorated TiO₂ Nanopillar Arrays. *Sci. Rep* **6**, 26670 (2016).

29. Wang, Y., Yu, J., Xiao, W. & Li, Q. Microwave-assisted hydrothermal synthesis of graphene based Au–TiO₂ photocatalysts for efficient visible-light hydrogen production. *J. Mater. Chem. A* **2**, 3847 (2014).

30. Chen, C., Zhai, Y., Li, F. & Ling, L. Photocurrent enhancement of the CdS/TiO₂/ITO photoelectrodes achieved by controlling the deposition amount of Ag2S nanocrystals. *Appl. Surf. Sci* **356**, 574–580 (2015).

31. Dong, W. *et al.* Facile synthesis of CdS@TiO₂ core–shell nanorods with controllable shell thickness and enhanced photocatalytic activity under visible light irradiation. *Appl. Surf. Sci* **349**, 279–286 (2015).

32. Zhang, W., Xiao, X., Zheng, L. & Wan, C. Fabrication of TiO₂/MoS₂@zeolite photocatalyst and its photocatalytic activity for degradation of methyl orange under visible light. *Appl. Surf. Sci* **358**, 468–478 (2015).

33. Tahir, K. *et al.* Visible light photo catalytic inactivation of bacteria and photo degradation of methylene blue with Ag/TiO₂ nanocomposite prepared by a novel method. *J. Photochem. Photobiol. B Biol* **162**, 189–198 (2016).

34. Xie, J. *et al.* Facile synthesis of hierarchical Ag₃PO₄/TiO₂ nanofiber heterostructures with highly enhanced visible light photocatalytic properties. *Appl. Surf. Sci* **355**, 921–929 (2015).

35. Xu, J.-W., Gao, Z.-D., Han, K., Liu, Y. & Song, Y.-Y. Synthesis of magnetically separable Ag₃PO₄/TiO₂/Fe₃O₄ heterostructure with enhanced photocatalytic performance under visible light for photoinactivation of bacteria. *ACS Appl. Mater. Interfaces* **6**, 15122–31 (2014).

36. Neves, M. C. *et al.* Photosensitization of TiO₂ by Ag₂S and its catalytic activity on phenol photodegradation. *J. Photochem. Photobiol. A Chem* **204**, 168–173 (2009).

37. Gholami, M., Qorbani, M., Moradlou, O., Naseri, N. & Moshfegh, A. Z. Optimal Ag₂S nanoparticle incorporated TiO₂ nanotube array for visible water splitting. *RSC Adv* **4**, 7838 (2014).

38. Shan, Z., Clayton, D., Pan, S., Archana, P. S. & Gupta, A. Visible Light Driven Photoelectrochemical Properties of Ti@TiO₂ Nanowire Electrodes Sensitized with Core–Shell Ag@Ag₂S Nanoparticles. *J. Phys. Chem. B* **118**, 14037–14046 (2014).

39. Ong, W. L., Lim, Y.-F., Ting Ong, J. L. & Ho, G. W. Room temperature sequential ionic deposition (SID) of Ag₂S nanoparticles on TiO₂ hierarchical spheres for enhanced catalytic efficiency. *J. Mater. Chem. A* **3**, 6509–6516 (2015).

40. Liu, X., Liu, Z., Lu, J., Wu, X. & Chu, W. Silver sulfide nanoparticles sensitized titanium dioxide nanotube arrays synthesized by *in situ* sulfurization for photocatalytic hydrogen production. *J. Colloid Interface Sci* **413**, 17–23 (2014).

41. Xie, Y., Heo, S. H., Kim, Y. N., Yoo, S. H. & Cho, S. O. Synthesis and visible-light-induced catalytic activity of Ag₂S-coupled TiO₂ nanoparticles and nanowires. *Nanotechnology* **21**, 15703 (2010).

42. Zhang, D., Xu, G. & Chen, F. Hollow spheric Ag-Ag2S/TiO₂ composite and its application for photocatalytic reduction of Cr(VI). *Appl. Surf. Sci* **351**, 962–968 (2015).

43. Li, Z., Xiong, S., Wang, G., Xie, Z. & Zhang, Z. Role of Ag₂S coupling on enhancing the visible-light-induced catalytic property of TiO₂ nanorod arrays. *Sci. Rep* **6**, 1–7 (2015).

44. Blanton, T., Misture, S., Dontula, N. & Zdzieszynski, S. *In situ* high-temperature X-ray diffraction characterization of silver sulfide, Ag₂S. *Powder Diffr* **26**, 114–118 (2012).

45. Shirke, B. S., Korake, P. V., Hankare, P. P., Bamane, S. R. & Garadkar, K. M. Synthesis and characterization of pure anatase TiO₂ nanoparticles. *J. Mater. Sci. Mater. Electron* **22**, 821–824 (2011).

46. Deepa, T. D. *et al.* Surfactant-assisted synthesis of porous TiO₂ nanofibers as an anode material for secondary lithium ion batteries. Sustain. *Energy Fuels* **238**, 37 (2017).

47. Moulder, J. F., Stickle, W. F., Sobol, P. E. & Bomben, K. D. Handbook of X-ray Photoelectron Spectroscopy 261 (1992).

48. Li, F. B., Li, X. Z. & Hou, M. F. Photocatalytic degradation of 2-mercaptobenzothiazole in aqueous La³⁺-TiO₂ suspension for odor control. *Appl. Catal. B Environ* **48**, 185–194 (2004).

49. Yang, D. *et al.* Synthesis of Ag/TiO₂ nanotube heterojunction with improved visible-light photocatalytic performance inspired by bioadhesion. *J. Phys. Chem. C* **119**, 5827–5835 (2015).

50. Park, K.-H. & Dhayal, M. High efficiency solar cell based on dye sensitized plasma treated nano-structured TiO_2 films. *Electrochem. commun* **11**, 75–79 (2009).

51. Jiang, D., Chen, L., Xie, J. & Chen, M. $Ag_2S/g-C_3N_4$ composite photocatalysts for efficient Pt-free hydrogen production. The co-catalyst function of Ag/Ag_2S formed by simultaneous photodeposition. *Dalt. Trans* **43**, 4878–85 (2014).

52. Chen, R., Nuhfer, N. T., Moussa, L., Morris, H. R. & Whitmore, P. M. Silver sulfide nanoparticle assembly obtained by reacting an assembled silver nanoparticle template with hydrogen sulfide gas. *Nanotechnology* **19**, 455604 (2008).

53. Fan, W., Jewell, S., She, Y. & Leung, M. K. H. *In situ* deposition of $Ag-Ag_2S$ hybrid nanoparticles onto TiO_2 nanotube arrays towards fabrication of photoelectrodes with high visible light photoelectrochemical properties. *Phys. Chem. Chem. Phys* **16**, 676–80 (2014).

54. Xu, C., Rangaiah, G. P. & Zhao, X. S. Photocatalytic degradation of methylene blue by titanium dioxide: experimental and modeling study. *Ind. Eng. Chem. Res* **53**, 14641–14649 (2014).

55. Dilpazir, S., Usman, M., Rasul, S. & Arshad, S. N. A simple UV-ozone surface treatment to enhance photocatalytic performance of TiO_2 loaded polymer nanofiber membranes. *RSC Adv* **6**, 14751–14755 (2016).

56. Lim, S. P, Pandikumar, A., Huang, N. M. & Lim, H. N. Enhanced photovoltaic performance of silver@titania plasmonic photoanode in dye-sensitized solar cells. *RSC Adv* **4**, 38111–38118 (2014).

57. Wei, N. *et al.* Ag_2O nanoparticle/TiO_2 nanobelt heterostructures with remarkable photo-response and photocatalytic properties under UV, visible and near-infrared irradiation. *Appl. Catal. B Environ* **198**, 83–90 (2016).

58. Xing, M., Li, X. & Zhang, J. Synergistic effect on the visible light activity of Ti^{3+} doped TiO_2 nanorods/boron doped graphene composite. *Sci. Rep* **4**, 5493 (2014).

59. Qiu, B. *et al.* Facile synthesis of the Ti^{3+} self-doped TiO_2-graphene nanosheet composites with enhanced photocatalysis. *Sci. Rep* **5**, 8591 (2015).

Acknowledgements

Author Contributions

S.G. designed the experiments, synthesized all the samples, did photocatalytic experiments, interpreted the results and wrote the initial manuscript with assistance from S.A. N.M. assisted in TEM and XPS studies. S.N.A. supervised the work, prepared all the figures, interpreted the results, reviewed and corrected the manuscript.

Additional Information

Supplementary information accompanies this paper at doi:10.1038/s41598-017-00366-7

Competing Interests: The authors declare that they have no competing interests.

Publisher's note: Springer Nature remains neutral with regard to jurisdictional claims in published maps and institutional affiliations.